
# Final Draft

## of the original manuscript

Fan, L.; Zhou, M.; Zhang, Y.; Dieringa, H.; Qian, X.; Zeng, Y.; Lu, X.; Huang, Y.; Quan, G.:

**Achieving high strength and ductility in a heterogeneous bimodal grain structured TiC/AZ61 magnesium nanocomposites via powder metallurgy**

In: Materials Science and Engineering: A. Vol. 867 (2023) 144344.

First published online by Elsevier: 18.11.2022

https://dx.doi.org/10.1016/j.msea.2022.144344

# Achieving high strength and ductility in a heterogeneous bimodal grain structured TiC/AZ61 magnesium nanocomposites via powder metallurgy

Lingling Fan[a,b,c], Mingyang Zhou[d], Yuwenxi Zhang[a,b], Hajo Dieringa[c], Xiaoying Qian[e], Ying Zeng[a,b,**], Xianwen Lu[a,b], Yuanding Huang[f], Gaofeng Quan[a,b,*]

[a] *Key Laboratory of Advanced Technologies of Materials, Ministry of Education, Sichuan, Chengdu 610031, PR China*

[b] *School of Materials Science and Engineering, Southwest Jiaotong University, Sichuan, Chengdu 610031, PR China*

[c] *Institute of Material and Process Design, Helmholtz-Zentrum Hereon, Geesthacht 21502, Germany*

[d] *Science and Technology on Reactor System Design Technology Laboratory, Nuclear Power Institute of China, Sichuan, Chengdu 610213, PR China*

[e] *College of Materials Science and Engineering, Chongqing University, Chongqing 400044, PR China*

[f] *Institute of Metallic Biomaterials, Helmholtz-Zentrum Hereon, Geesthacht 21502, Germany*

## Abstract

Heterogeneous TiC/AZ61 nanocomposites, consisting of TiC-rare coarse grain (CG) bands and TiC-rich fine grain (FG) zones, were fabricated to simultaneously improve the strength and ductility of nanoparticles reinforced Mg matrix composites. The fraction of CG bands could be optimized by adjusting the mechanical ball milling time to change the proportion of powders with different morphologies. It was found that composites began to form a heterogeneous bimodal grain (HBG) structure after 12 h ball milling. With further increasing the ball milling time from 12 h to 30 h, the proportion of spherical powder decreased, the volume fraction of CG bands decreased from 48.4% to 11.7%. Excellent comprehensive mechanical properties (ultimate tensile strength: 417 MPa, yield strength: 323 MPa, and elongation: 10.2%) were achieved for the composite with ~25 vol.% CG bands after 20 h of ball milling. Moreover, the HBG-20 h composite had significant additional strengthening at ultimate tensile strength owing to the existence of geometrically necessary dislocations (GNDs) inside the coarse grain bands, which were introduced by mechanical incompatibility between the CG band and FG zone. Such dislocations provided optimum back-stress work hardening at the HBG-20 h composite due to its suitable CG band fraction (~ 25 vol.%), contributing to the high strain-hardening.

## Keywords:

TiC/AZ61 composites; Heterogeneous bimodal grain structure; Strengthening mechanism; Increasing ductility mechanism

Corresponding authors:

E-mail address: quangf@swjtu.edu.cn (G.F. Quan), clzy@swjtu.edu.cn (Y. Zeng)

## 1. Introduction

Particulate-reinforced metal matrix composites (PRMMCs) can be regarded as lightweight and energy-efficient design strategies for the next generation of advanced structural materials [1]. To achieve maximum strengthening, a great deal of research attempted to obtain the homogeneous dispersion of the nanoparticles through special dispersion processes or surface modification of the reinforcements [2, 3]. Unfortunately, conventional PRMMCs always face the well-known challenge of compromising strength and ductility, which greatly limits their practical applications [4].

In recent years, different heterogeneous structural designs were introduced to overcome the dilemma of strength-ductility of composite, including inverse nacre structured [5], functionally-graded grain [6], bioinspired structure [7,8], spatial arrays of nanoparticles [9]. Another potential effective approach is to design heterogeneous bimodal grain (HBG) structures [10]. HBG structure introduces coarse grains (CG) into high-strength materials consisting mainly of fine grains (FG) or even nano-grains to increase the plasticity of the materials. Liu et al. [11] prepared a heterogeneous bimodal carbon nanotube (CNT)/Al-Cu-Mg composite by powder metallurgy combined with subsequent hot extrusion, attaining more than 100% increase in ductility and almost no loss of ultimate tensile strength compared to the uniform CNT/Al-Cu-Mg composite. The increase in elongation was due to the introduction of CG, which facilitated strain transfer and thus alleviated stress concentration. In addition, the CG areas could resist the development of microcracks. Ma et al. [12] fabricated heterogeneous bimodal and uniform CNT/2009Al composites. They found that a heterogeneous composite exhibited an 88% increase in elongation and a 2% increase in tensile strength compared to the uniform composite. In addition, the bimodal grain structure in magnesium alloys has also proven beneficial for achieving excellent comprehensive mechanical properties. Wang et al. [13] found that the mechanical properties of bimodal Mg-9Al-1Zn (wt.%) alloy (UTS: 371 MPa, EL: 26.4%) were much higher than that of the conventional AZ91 alloy. Zhang et al. [14] found that the bimodal structure sample had higher tensile strength and uniform elongation than the fine-grained sample in the Mg-8Al-2Sn-1Zn alloy. Therefore, magnesium matrix composite with the HBG structure is promising to break the strength-plasticity dilemma.

However, extremely few reports were published on magnesium matrix composites with HBG structure [15,16]. Xiang et al. [15] prepared graphene nanoplatelets (GNPs)/Mg-6Zn composites by semi-solid stirring followed by hot extrusion. They had a heterogeneous bimodal microstructure due to the non-uniform distribution of GNPs. Compared with the monolithic alloy, the nanocomposites exhibited an increased yield

strength and ultimate tensile strength by 166% and 35%, respectively, as well as high ductility (~6.3%). The authors attributed the improvement of mechanical properties to the particular HBG microstructure. The authors thought that the loss of ductility in composites could be improved by strain hardening provided by dislocation activity in the CG region. But no relevant evidence and further analysis were provided. Shen et al. [16] prepared Mg matrix composites with high strength (UTS: ~402 MPa, YS: ~323 MPa) and good ductility (~8.3%) by semi-solid stirring followed by hot extrusion. The main reason for the improved mechanical performance was the formation of a bimodal grain microstructure by adding bimodal-size SiC particles. The fine grains were produced through the particle stimulation of nucleation and the pinning effect of grain boundaries. The coarse grains were formed in these regions with sparse $SiC_p$ distribution. The authors speculated that ensuring good ductility was related to the presence of CGs. The CG zones could enhance the strain hardening and act as a crack arrester, thus improving the ductility of the composites, but no relevant evidence was given. According to the research of Xiang et al. [15] and Shen et al. [16], the formation of HBG structure in their magnesium matrix composites was due to the non-uniform distribution of reinforcement. It is difficult to regulate and optimize the HBG microstructure by semi-solid stirring subsequent extrusion. However, no literature on HGB magnesium matrix composites currently reports that a controllable method could be used to optimize the HGB microstructure. In addition, some studies have shown that the microstructure parameters significantly influence the mechanical properties of the HGB composites, especially the fraction of coarse grains [11,17]. Therefore, it is necessary to use a more feasible process to control and optimize this microstructure.

In summary, current research on HBG Mg matrix composites suffered from the following problems. (i) No further microstructure optimization of the HBG Mg matrix composites has been carried out to achieve optimum mechanical properties. (ii) The mechanisms responsible for strengthening and improving the ductility in HBG Mg matrix composites were not clarified.

In this work, we used the conventional powder metallurgy route followed by hot extrusion to fabricate heterogeneous TiC/AZ61 composites with inhomogeneous TiC distribution and grain size. The heterogeneous TiC/AZ61 composite consisted of TiC-rare coarse grain (CG) bands and TiC-rich fine grain (FG) zones. The fraction of CG bands was regulated by mechanical ball milling time. The aim is to (i) develop TiC/AZ61 nanocomposites with much higher strength-ductility through the optimal heterogeneous structure design and (ii) clarify the mechanisms responsible for strengthening and ductilizing.

## 2. Experimental procedures

## 2.1. Raw materials

The spherical AZ61 magnesium alloy powders with an average diameter of 70 μm and purity of 99.9% were used as the alloy matrix (Fig. 1(a)). These powders were supplied by CHINO New Material Technology Co., Ltd., China. TiC nanoparticles (average size about 50 nm) were applied as reinforcements supplied by Shanghai ST-nano Science & Technology Co. Ltd., China. Fig. 1(b) and (c) show TEM image, corresponding electron diffraction pattern and XRD pattern of TiC nanoparticles.

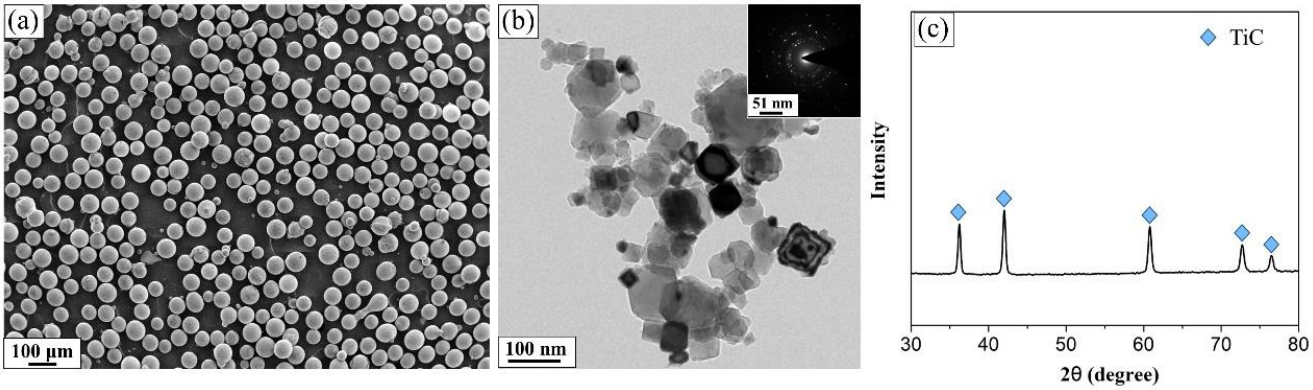


**Fig. 1.** (a) SEM image of AZ61 powders, (b) TEM image of TiC nanoparticles, (c) XRD pattern of TiC nanoparticles.

## 2.2. Preparation of composites

1 wt.% TiC, AZ61 powders and 1 wt.% stearic acid (used as a process control agent to prevent cold welding) were first added to a stainless-steel container. This step was carried out in a glove box filled with Ar atmosphere. The container was subsequently filled with Ar gas. The ball milling process was conducted using a PBM-4A planetary mill with a ball milling speed of 150 rpm. Different ball milling time were used, i.e., 2 hours, 6 hours, 12 hours, 20 hours, and 30 hours, respectively. The grinding medium was stainless steel balls. The ball-to-powder ratio was set at 20:1. The ball mill was stopped for 10 min after every 30 min to prevent overheating. The container was filled with Ar atmosphere every 30 min to minimize oxidation. After the ball milling, the milled composite powders were cold-pressed into Φ45 mm billets at a pressure of 650 MPa for 7 min and then sintered together with the mold under the protection of the Ar atmosphere at 520 ℃ for 2 h. After sintering, the mold was cooled down to 400 ℃. The compacts were hot-pressed at 300 MPa for 15 min. Finally, hot extrusions were carried out at 350 ℃ with an extrusion ratio of 20:1. All the hot-pressed compacts were extruded into Φ10 mm rods. The monolithic AZ61 rods were prepared using AZ61 powder without the ball milling process and the rest of the preparation steps were the same as for the composite.

## 2.3. Materials characterization

Ball-milled powders and composites microstructures were observed using optical microscopy (OM, ZEISS), scanning electron microscope (SEM, JSM 7800F) equipped with an energy dispersive spectroscope (EDS, Oxford X-MAX 80) and transmission electron microscope (TEM, FEI Talos F200X). The microstructure of the composite after straining was also investigated by TEM. The specimens for OM observation were mechanically ground till to the 2500# SiC abrasive papers, then polished and etched in the acetic-picral solution (4.2 g picric acid, 10 mL acetic acid, 100 mL ethyl alcohol, and 10 mL distilled water) for 8 s. The TEM foils were prepared by grinding-polishing to a thickness of 50 μm, followed by ion beam thinning (Gatan 695). The CG fraction and the proportion of undeformed spherical powders in the ball-milled powders were evaluated using image-Pro Plus software based on at least three OM and SEM images, respectively.

Electron backscatter diffraction (EBSD) scans were executed on a JEOL JSM-7800F SEM equipped with Oxford C-Nanosystem and EBSD detector. The specimen for EBSD analysis was treated by argon ion-milling (IM4000PLUS). Texture measurement was carried out by X-ray diffractometer (XRD, Bruker D8 Discover) with Cu Kα radiation on a circular section perpendicular to the direction of extrusion.

The uniaxial tensile tests were carried out at a strain rate of $1\times 10^{-3}s^{-1}$ at room temperature using a universal testing machine (MTS-CMT5105, SANS). The dog bone-shaped specimens with a diameter of 3 mm and a gauge length of 15 mm were machined from the extrusion rods with the axis parallel to the extrusion direction. Three samples were tested for each composite. The densities of the matrix and composites were determined using the DX-100E fully automatic electronic densitometer (accuracy $10^{-4}$ g) and distilled water as the soaking solution. The samples were polished before testing and 3 parallel samples of each composite were selected. The theoretical densities of the composites were estimated by the rule-of mixture principle. The microhardness was measured with a Vickers hardness tester at a load of 200 gf and a dwell time of 15 s. The number of micron indentations during the test was 12. A nanoindentation tester (KEYSIGHT G200) was conducted to measure the intrinsic mechanical properties of the nanocomposite at a maximum displacement of 1.5 μm and a dwell period of 5 s. The indenter of nanoindentation is a triangular pyramid Berkovich diamond indenter. The number of nano indentations during the test was 20.

## 3. Results

### 3.1. Powder morphology and nanoparticle distribution

Fig. 2 shows the morphology evolution of the powders as the ball milling time increased. During the ball milling process, AZ61 powders underwent plastic deformation, became flat and finally broke. The proportion

of deformed powders noticeably increased and the proportion of undeformed spherical powder decreased correspondingly. The distribution of reinforcements plays an important role in the properties of the composites. Fig. 3 shows the evolution of TiC nanoparticles distribution in the composite powders at different ball milling time. After ball milling for 2 h, the agglomeration of nanoparticles was apparent (marked by the yellow dashed ellipse, Fig. 3(a)). With the increase of ball milling time, the nanoparticles (marked by yellow arrows) gradually dispersed uniformly. Moreover, they decreased and became smaller on the powder surface. During milling, they were pressed into the matrix powder, which was beneficial for avoiding their agglomeration on the powder surface. Fig. 4 shows SEM image and EDS mapping of composite powder after milling for 20 h. Based on the SEM image and element mapping, the white nanoparticles marked by yellow arrows in (Fig. 4(a)) corresponded to TiC nanoparticles. Fig. 5 shows SEM image and corresponding EDS mapping of the final TiC/AZ61 composite after different ball milling time. It reveals that increasing ball milling time resulted in a more uniform dispersion of the Al-rich phase and TiC nanoparticles. According to previous studies on AZ series magnesium alloys and magnesium matrix composites, these Al-rich phases were β-$Mg_{17}Al_{12}$ phases [18,19].

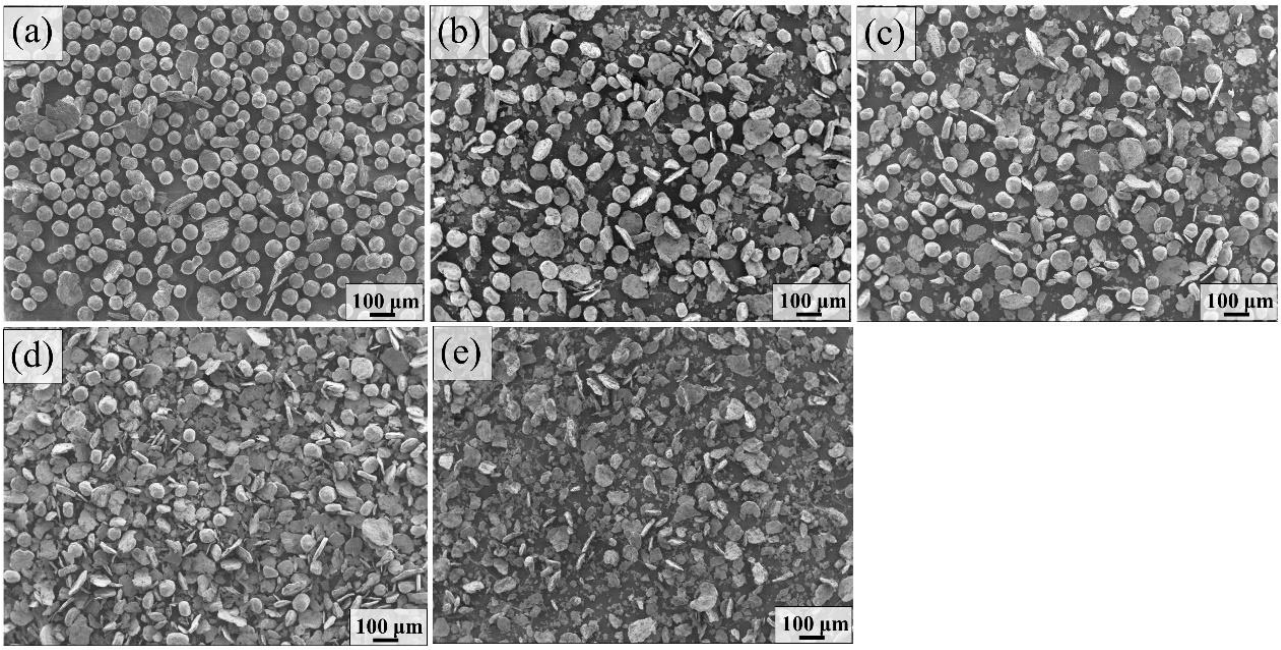


**Fig. 2.** SEM images showing particle morphology of TiC/AZ61 composite powders after different ball milling time: (a) 2 h, (b) 6 h, (c) 12 h, (d) 20 h, (e) 30 h.

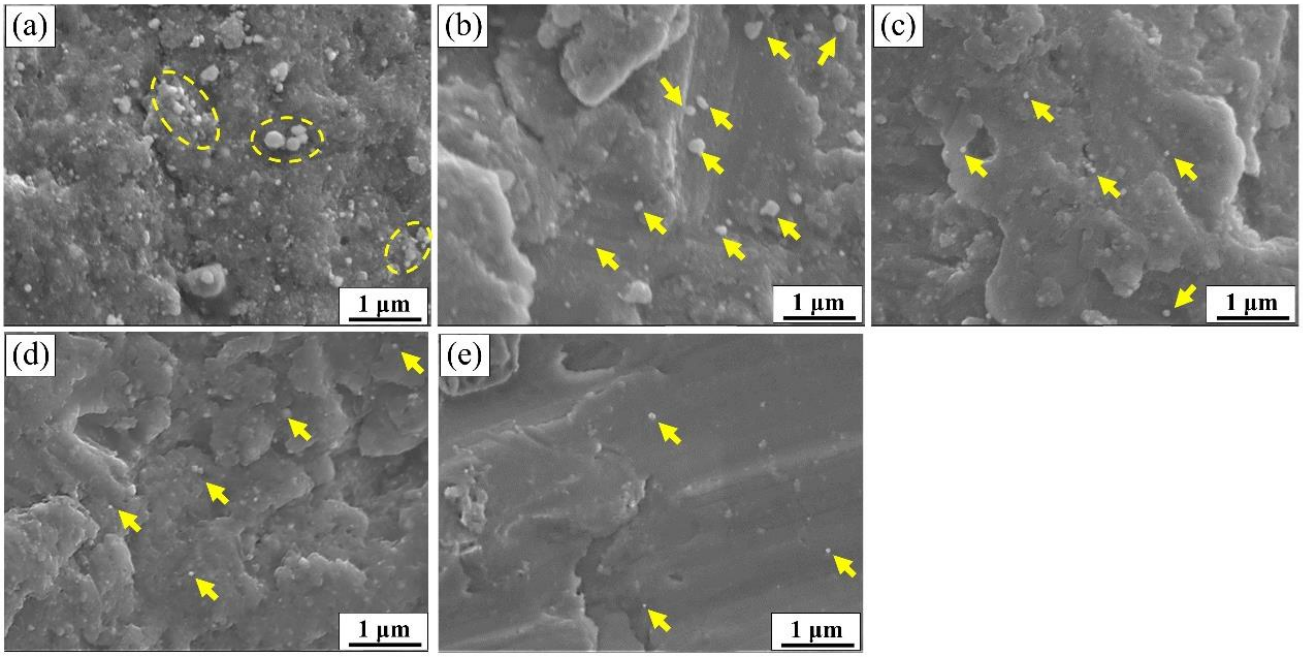


**Fig. 3.** Evolution of TiC nanoparticles distribution in the composite powders: (a) 2 h, (b) 6 h, (c) 12 h, (d) 20 h, (e) 30 h.

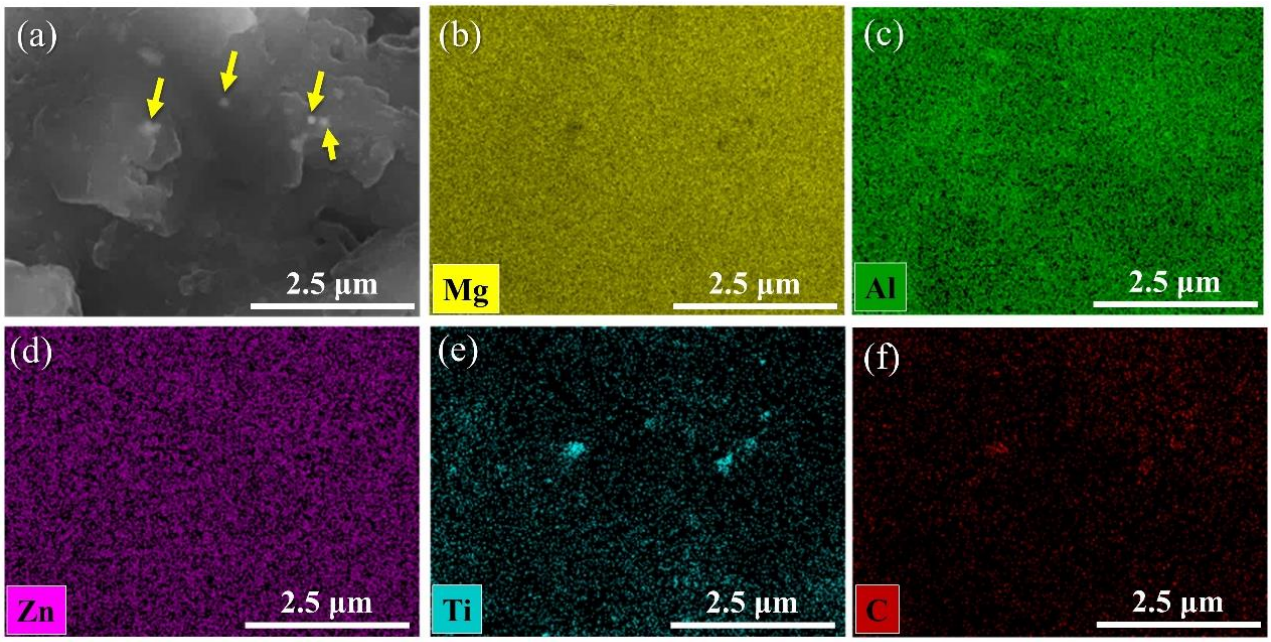


**Fig. 4.** (a) SEM image of composite powder after milling for 20 h, (b)-(f) corresponding EDS mapping of Mg, Al, Zn, Ti, and C, respectively.

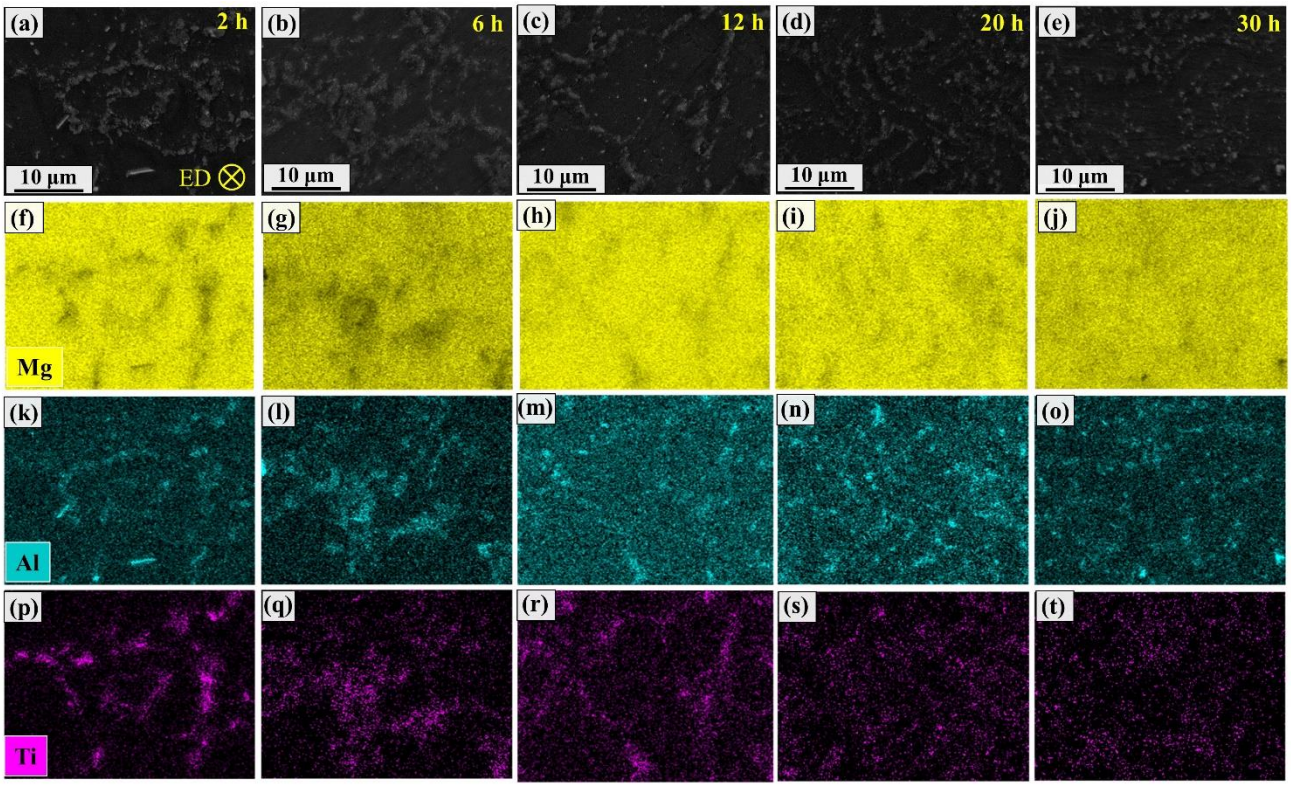


**Fig. 5.** SEM image of the final TiC/AZ61 composite after different ball milling time: (a) 2 h, (b) 6 h, (c) 12 h, (d) 20 h, (e) 30 h; corresponding EDS mapping of Mg (f-j), Al (k-o) and Ti (p-t), respectively.

### 3.2. Microstructural evolution

Fig. 6 shows the OM images of the TiC/AZ61 composites with different milling time. As shown by these OM images (Fig. 6 (a)-(e)), the bright regions decreased and the black areas increased as the ball milling time increased. By further magnification, as shown in Fig. 6 (f)-(j), it can be demonstrated that the bright regions included coarse grains. According to the previous investigation [11], the black areas corresponded to the fine-grained regions, which were more susceptible to chemical corrosion because of the higher percentage of grains and phase boundaries. Fig. 7 (a) shows the variation in the percentage of undeformed spherical powders and the proportion of CG bands of the composite with the milling time. It reveals a positive correlation between them, demonstrating that the CG bands and FG zone should mainly originate from undeformed and deformed powders, respectively. After 2 h and 6 h of ball milling, the microstructure of the composites was composed mainly of coarse grains, so they are named CG composites. After 12 h of ball milling, the CG bands fraction of the composite was less than 50% and microstructure was mainly composed of fine grain. Thus, the HBG structure began to form. So, the composites ball-milled for 12 h, 20 h and 30 h were named HBG-12 h, HBG-20 h and HBG-30 h composites, respectively. Fig. 7 (b) shows the size of CG bands as a function of milling time for the HBG composites. The corresponding statistical results are listed in Table 1. Increasing the ball milling time

decreased the fraction, width and length of the CG bands.

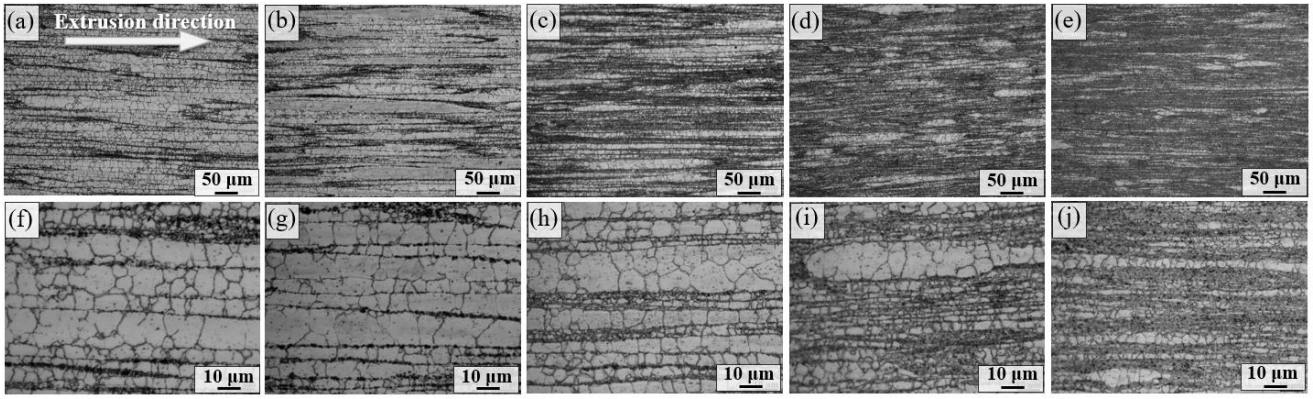


**Fig. 6.** OM images of TiC/AZ61 composites with different ball milling time: (a) (f) 2 h, (b) (g) 6 h, (c) (h)12 h, (d) (i) 20 h, (e) (j)30 h.

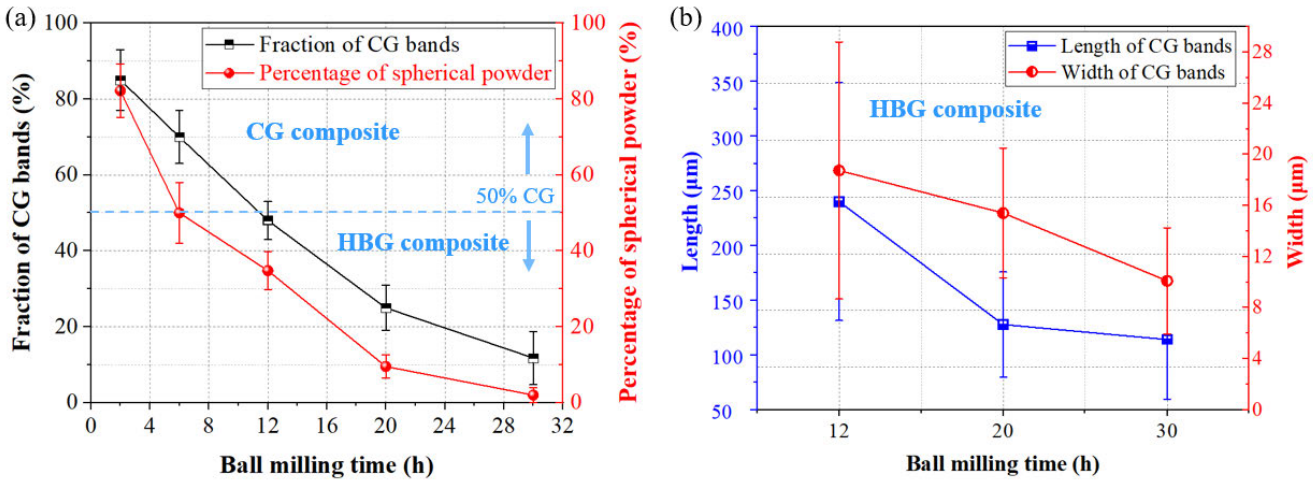


**Fig. 7.** (a) Variation in the percentage of undeformed spherical powders and the fraction of CG bands in the composite with the ball milling time, (b) the length and width of the CG bands in different HBG composites.

**Table 1** Statistical results of coarse grain bands.

| Composites | Width (μm) | Length (μm) | Fraction (%) |
|---|---|---|---|
| HBG-12 h | 18.7 | 240.2 | 48.4 |
| HBG-20 h | 15.4 | 128.0 | 25.1 |
| HBG-30 h | 10.1 | 114.2 | 11.7 |

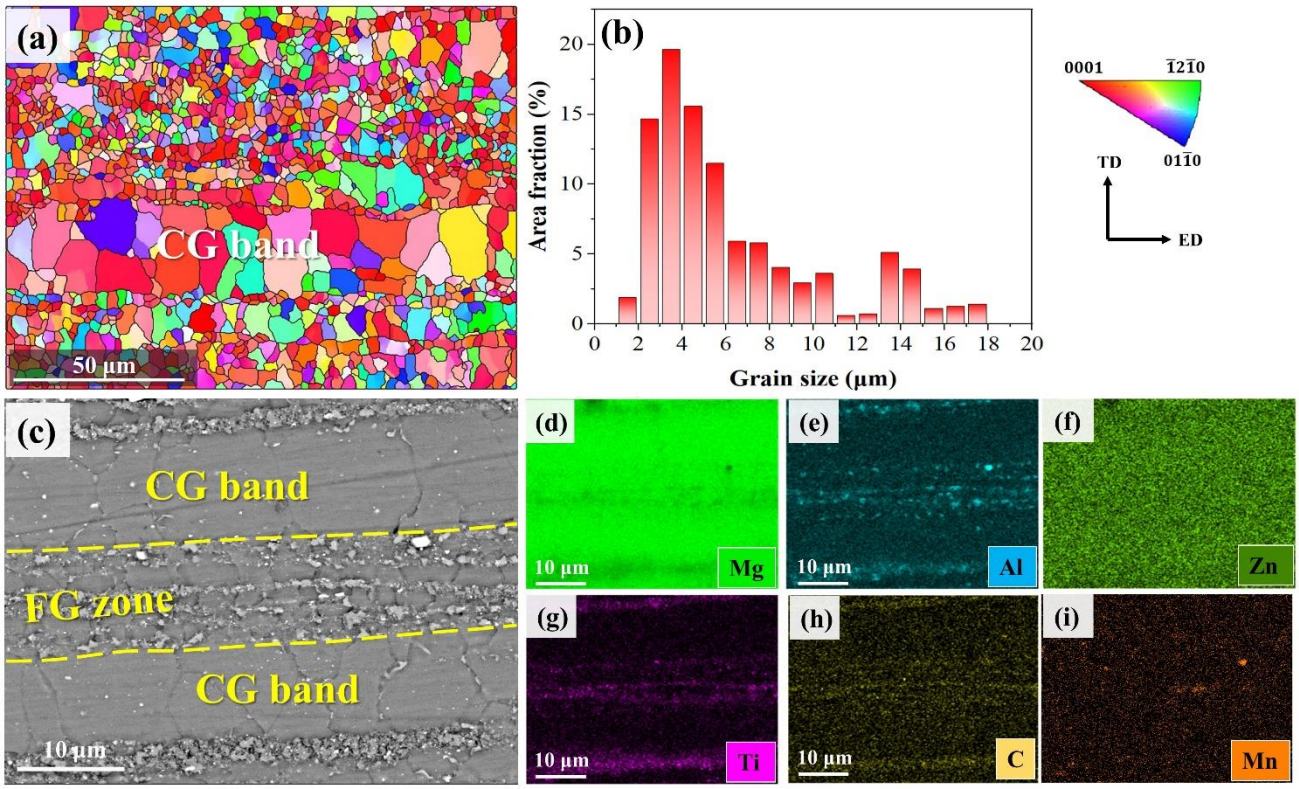


**Fig. 8.** Representative EBSD/BSEM images of HBG-20 h composite: (a) inverse pole figure (IPF) maps, (b) corresponding area fraction of grains with different sizes, (c) backscattered SEM image, (d)-(i) EDS mapping of Mg, Al, Zn, Ti, C and Mn, respectively.

To further analyze microstructural features of heterogeneous composites, EBSD tests, Backscattered SEM, EDS and TEM were conducted, and the corresponding results are shown in Fig. 8 and Fig. 9. Both Fig. 8 (a) and (b) well reveal the bimodal grain structure in the heterogeneous composite. Some coarse grains gathered together to form a CG band embedded in the fine grain zone, which was consistent with that shown in Fig. 6(d) and (i). Fig. 8 (c) clearly indicates the particles were sparse in the CG band, whereas they were rich in the FG zone. The corresponding EDS mapping demonstrates that these particles were mainly composed of β-$Mg_{17}Al_{12}$, TiC and Al-Mn intermetallics. In previous studies on AZ series magnesium alloys, different types of Al-Mn phases, such as $Al_{11}Mn_4$ or $Al_8Mn_5$, have also been discovered [20,21]. It can be found that the distribution of TiC nanoparticles was similar to that of the β-$Mg_{17}Al_{12}$ phase. It is because the nano reinforcement could act as heterogeneous nucleus substrates, efficiently stimulating the nucleation process of β-$Mg_{17}Al_{12}$ phase [22]. Fig. 9 (a) shows that the nanoparticles were also rich in the FG zone but rare in the CG region. Figs. 9 (a-c) prove that TiC nanoparticles mainly located in the particle-rich FG region. And there was a trace of Al-Mn nanophases. Therefore, heterogeneous TiC/AZ61 nanocomposite consisted of TiC-rare coarse grain (CG) bands and TiC-rich fine grain (FG) zones. HRTEM images in Fig. 9 (f) and (g) indicate that the interfaces of TiC/Mg had no

obvious defects and no reaction layer. The interfacial bonding was clean and good. The crystal plane spacing at two sides was 0.192 nm and 0.217 nm, respectively, corresponding to Mg (102) and TiC (200) crystal planes.

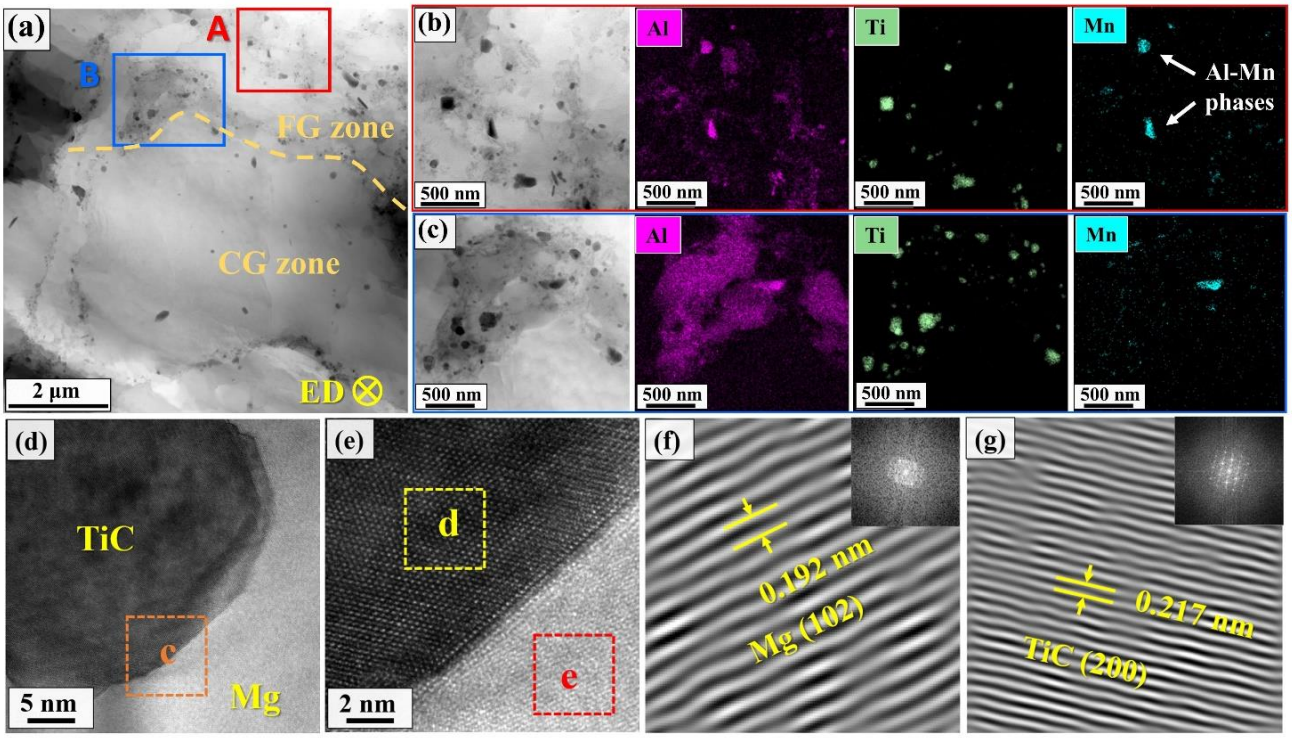


**Fig. 9.** (a) TEM image of the HBG-20 h composite shows nanoparticle distribution. (b) is the enlarged view of the red box "A" in (a) and its corresponding EDS mapping. (c) is the enlarged view of the blue box "B" in (a) and its corresponding EDS mapping. (d) HRTEM image shows a TiC nanoparticle in matrix. (e) is the squared region "c" in (d), showing the interface between Mg and TiC. (f) inverse fourier transform corresponding to the yellow squared region "d" in (e). (g) inverse fourier transform corresponding to the red squared region "e" in (e).

Texture has an obvious effect on the plasticity of magnesium alloy. In this study, the texture evolution of the TiC/AZ61 composites with different ball milling time was analyzed by XRD. Fig. 10 shows the $\{0001\}$ and $\{10\bar{1}0\}$ pole figures of TiC/AZ61 composites at various ball milling time. It indicates that the composites at different milling time had similar fiber textures with $\langle 10\bar{1}0\rangle$ // ED. The previous investigation showed that the fiber texture of magnesium alloys exhibited the preferential basal plane orientation, i.e., $\langle 10\bar{1}0\rangle$ // ED, that is, $\{0001\}$ basal plane and $\langle 10\bar{1}0\rangle$ grain were parallel to the extrusion direction [23]. As shown in Fig. 10, the texture intensity remained relatively stable with different ball milling time. Therefore, its influence on the mechanical properties could be ignored in the present work.

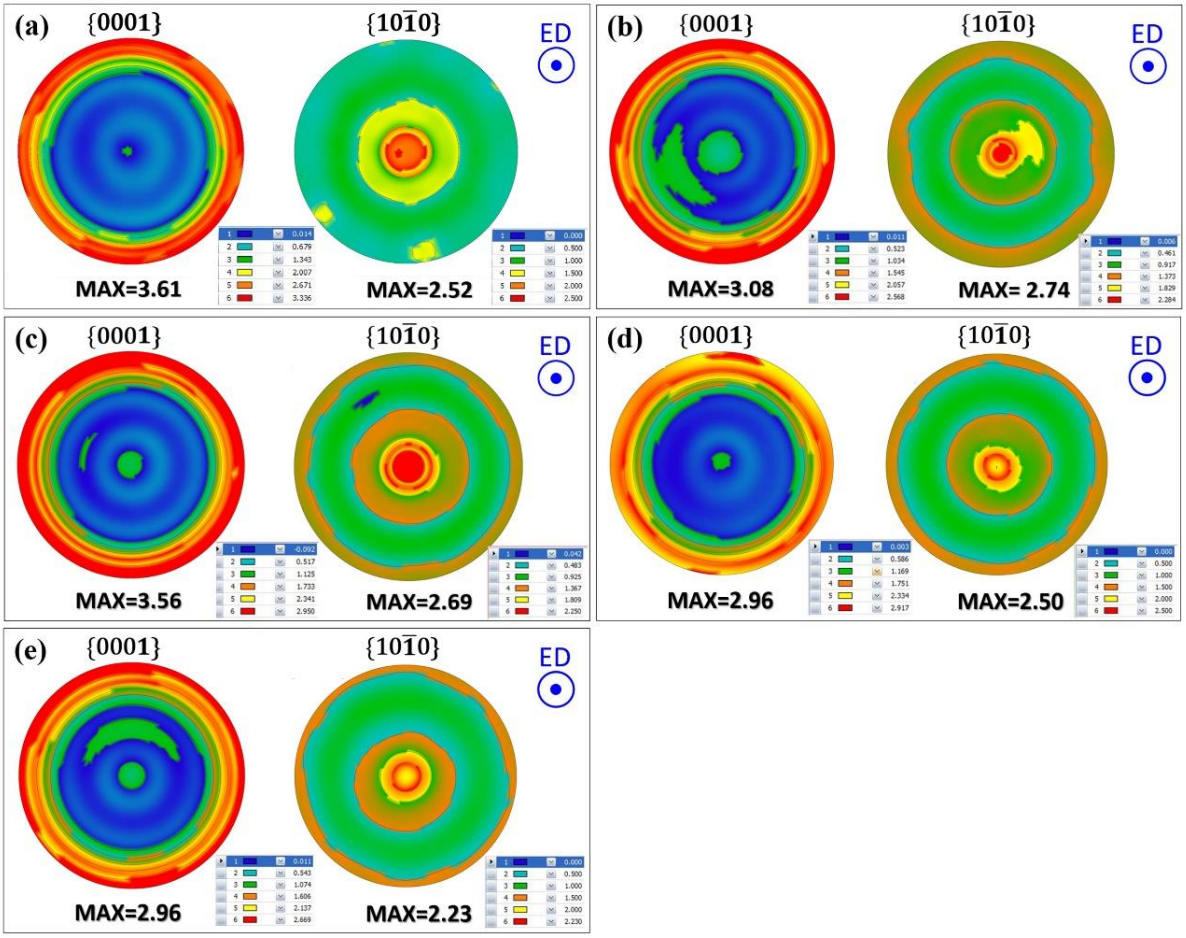


**Fig. 10.** {0001} and {10$\bar{1}$0} pole figures of TiC/AZ61 composites: (a) 2 h, (b) 6 h, (c) 12 h, (d) 20 h, (e) 30 h.

### 3.3. Mechanical properties

Figs. 11 (a) and (b) show the mechanical performances of AZ61 and TiC/AZ61 composites. Fig. 11 (c) shows the microhardness and relative densities of TiC/AZ61 composites. The exact values of yield strength (YS), ultimate tensile strength (UTS), elongation (El), microhardness and relative density are listed in Table 2. In this study, yield stress is the stress value corresponding to 0.2% plastic strain. With the increase of ball milling time, as shown in Figs. 11 (a) and (b), the YS increased continuously, while UTS first increased from 2 h to 20 h and then decreased at 30 h. The elongation did not show a monotonous downward trend but presented an inflection point at 20 h. The reasons will be analyzed carefully in the discussion sections. Therefore, the composite with excellent performance was obtained when the ball milling time reached 20 h. It had high strength (YS: 323 MPa, UTS: 417 MPa) and good ductility (~10.2%). As indicated by Fig. 11 (c), the relative density of composites increased as the ball milling time increased. In addition, the microhardness exhibited a gradually growing trend ascribed to grain refinement, as evidenced by Fig. 6.

Fig. 11 (d) shows the nanoindentation load-depth curves for the CG band and FG zone in the HBG-20 h composite. The mechanical properties based on the nanoindentation tests are summarized in Table 3. Apparently, the CG and FG zones showed different mechanical properties. The hardness and elastic modulus of FG zones were much higher than that of CG zones.

Fig. 11 (e) shows the mechanical properties of HBG-20 h composite in this study and other magnesium matrix nanocomposites in previous research [15,16,24-45]. Most nanocomposites exhibited a strength-ductility dilemma, with data points located below a typical "banana-shaped" curve, although some of them were prepared using new or specially modified processes. For example, the composites marked with yellow circles were prepared using a surface modification process to avoid the agglomeration of the reinforcements and to make these reinforcements as homogeneously dispersed as possible [32,40,41,45]. The aim of preparing composites marked with green circles was to achieve their strengthening and toughening by modifying the spatial distribution of reinforcements (the fiber-like arrays) [27,28]. The fiber-like array as a whole reinforcement could significantly improve the load-carrying capacity of $TiB_2$ nanoparticles. The composites indicated by the blue arrows were reported to have a bimodal grain structure, which was formed owing to the non-uniform distribution of reinforcements [15,16]. Unfortunately, although these composites had such promising structures, their mechanical properties were still under the banana line because the bimodal grain structures of their composites were not optimized. In contrast, the mechanical properties of the present HBG-20 h composite have overcome the reported strength-ductility dilemma, demonstrating that the HBG structure optimized by ball milling and extrusion was an effective approach to enhance the strength-ductility synergy.

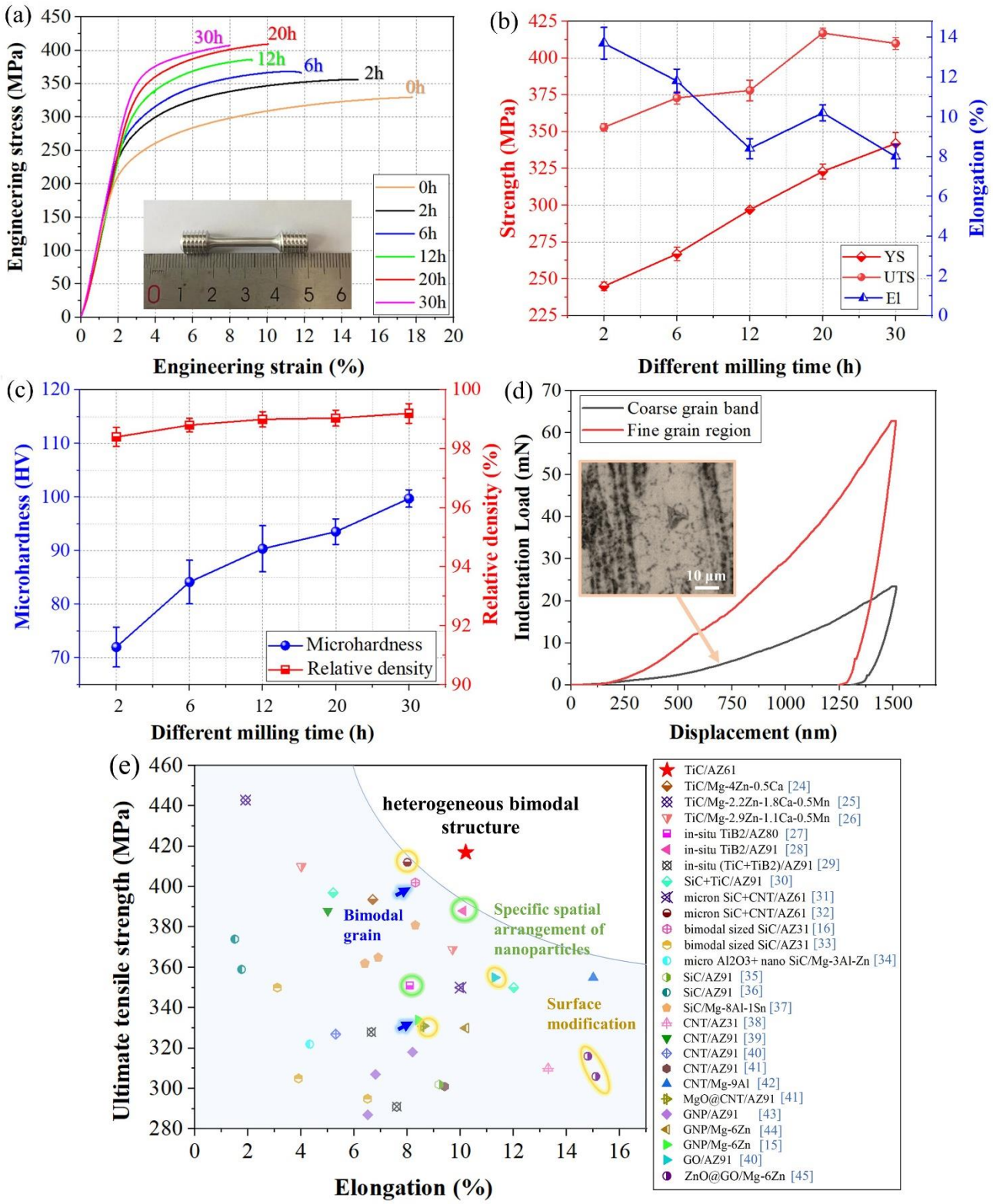


**Fig. 11.** (a) Engineering tensile stress-strain curves of AZ61 and its composites with different ball milling time, (b) mechanical properties values of TiC/AZ61 composites vs. ball milling time, (c) curves of microhardness and relative density, (d) nanoindentation load-displacement curves of the FG zone and CG band in the HBG-20 h composite, (e) tensile properties of HBG-20 h composite in this study and other magnesium matrix

nanocomposites in previous research [15,16,24-45].

**Table 2** Mechanical properties of AZ61 matrix and TiC/AZ61 composites.

| Materials | Ball milling time (h) | Tensile properties | | | Microhardness (HV) | Relative density (%) | Structure |
|---|---|---|---|---|---|---|---|
| | | YS (MPa) | UTS (MPa) | El (%) | | | |
| AZ61 | 0 | 207.3±2.4 | 329.5±3.7 | 17.8±0.5 | / | / | CG |
| TiC/ AZ61 | 2 | 245.4±3.0 | 353.3±2.5 | 13.7±0.9 | 72.2±3.7 | 98.5±0.32 | CG |
| | 6 | 266.7±4.6 | 367.4±4.3 | 11.8±0.7 | 84.5±4.1 | 98.9±0.23 | CG |
| | 12 | 296.6±1.1 | 377.6±7.1 | 8.4±0.6 | 90.1±4.3 | 99.3±0.26 | HBG |
| | 20 | 322.8±5.1 | 417.1±3.6 | 10.2±0.5 | 93.7±2.4 | 99.3±0.27 | HBG |
| | 30 | 342.2±7.3 | 410.0±4.0 | 8.0±0.7 | 100.4±1.6 | 99.1±0.33 | HBG |

**Table 3** Nanoindentation properties of the FG and CG zones in HBG-20 h composite.

| Zones | Hardness (GPa) | Elastic modulus (GPa) |
|---|---|---|
| CG | 0.7±0.14 | 41.1±5.59 |
| FG | 1.2±0.09 | 55.5±2.56 |

## 4. Discussion

### 4.1 Effect of ball milling on TiC nanoparticle distribution and microstructure

According to the previous analysis on Fig. 7, it is considered that the CG bands and the FG zone derived from the undeformed spherical powder and deformed powder, respectively. Fig. 12 (a) shows schematic diagram of microstructure of extruded composite formed by powders of different shapes. The mechanism diagram is shown in. For the spherical powder, the reinforcement dispersed on the surface of the powder. In the subsequent sintering and hot-pressing process, the micropores between powder particles eliminated and then nano-TiC located at the "particles" boundary. After extrusion, the "equiaxed particles" were elongated, meanwhile dynamic recrystallization and growth of grains inside the "particles" occurred. Because the nano - TiC located at the "particle" boundary, the grain growth inside the "particle" could not be impeded, resulting in the formation of TiC-rare CG bands. However, for flake powders, their large and flat surface facilitated the uniform dispersion of the reinforcement and allowed more nanoparticles to be accommodated. In addition, their thin thickness enabled the nano-TiC to be easily pressed into the interior of the powder. In the subsequent thermal process, many nano-TiC inside "particle" could pin the grain boundaries and thus prevent grain growth, resulting in TiC-rich FG zones. Therefore, the powder morphology had an essential influence on the reinforcement distribution, which further affected the microstructure of the final composite.

Fig. 12 (b) shows schematic diagram of the effect of ball milling time on reinforcement distribution and

microstructure after extrusion. When the ball milling time was short (2 h and 6 h), the ball milled powder was mainly composed of spherical powder, including a small amount of flaky powder. So, the final composite was primarily comprised of coarse grains. The spatial distribution of TiC nanoparticles in extruded composite was very heterogeneous. They showed linear agglomerates from parallel to the extrusion direction and clustering near the boundary of the CG zone from perpendicular to the extrusion direction. When the ball milling time was long (12 h, 20 h and 30 h), the ball milled powder was mainly made up of flake powder, containing part of spherical powder. Thus, their microstructure consisted of a high number of FG zones and some CG bands (i.e., HBG structure). With the increase of milling time, the proportion of spherical powder decreased continuously, so the fraction of CG bands in the final composite decreased. The spatial distribution of TiC nanoparticles in extruded composite was uneven on the whole but was uniform in the local (FG region). The TiC nanoparticle distribution in the FG region of the HBG-12h (Fig. 5 (r)) and HBG-20h (Fig. 5 (s)) composites is uneven and uniform, respectively. It indicated that sufficient ball milling time was required to make the particle distribution in the FG region homogeneous. Therefore, adjusting the ball milling time was a controllable preparation method to obtain the HBG structure and further optimize it. The fraction of CG bands in the HBG composite could be controlled by regulating the ball milling time to change the proportion of powders with different morphologies.

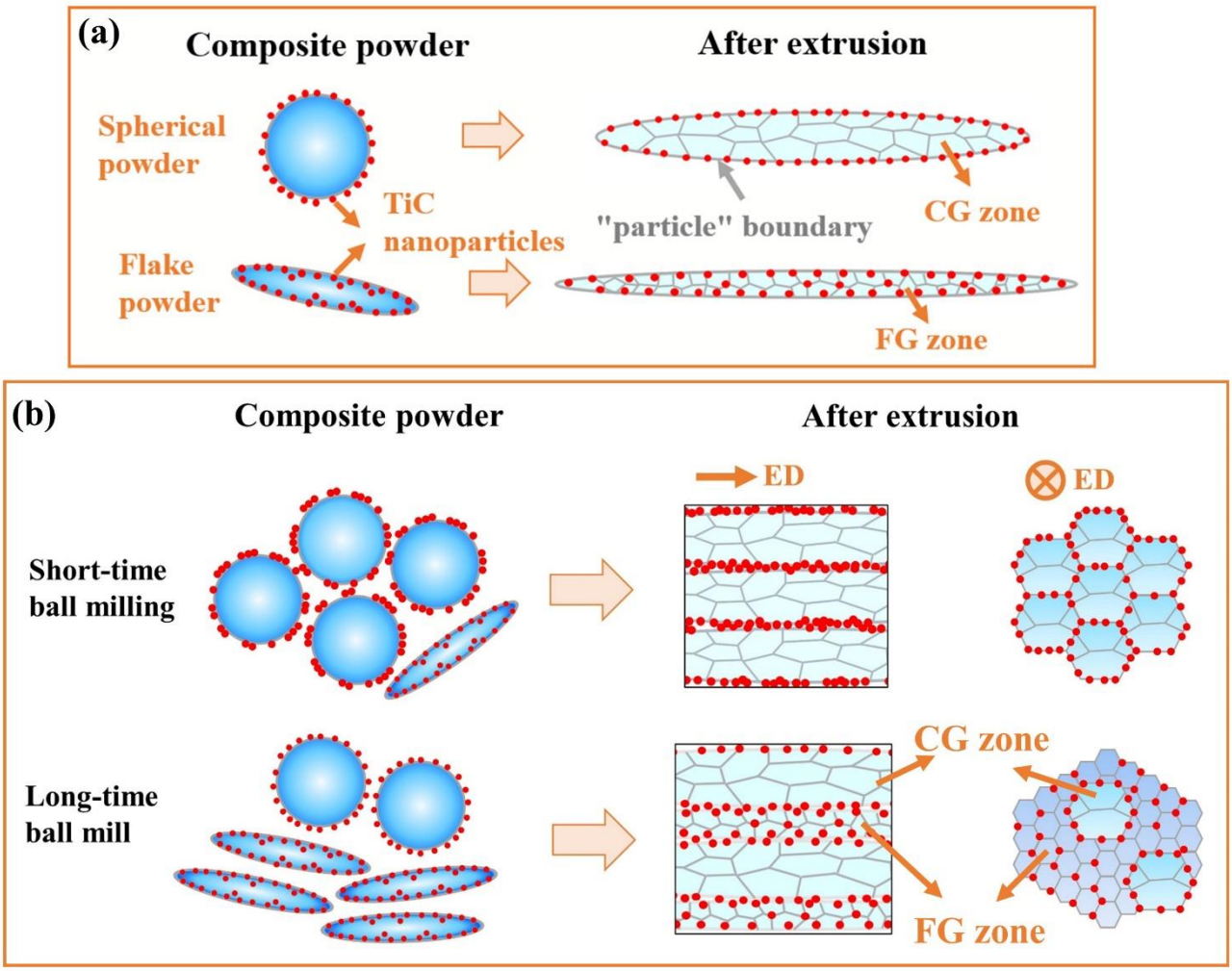


**Fig. 12.** (a) Schematic diagram of microstructure of extruded composite formed by powders of different shapes, (b) schematic diagram of the effect of ball milling time on reinforcement distribution and microstructure of extruded composites.

### 4.2. Effect of ball milling time on the mechanical properties of composites

The influence of the ball milling time on the mechanical properties of composites are mainly considered from the following aspects: dispersion and structural integrity of the reinforcement, relative density and grain size [46-49]. According to the present results, an increase in ball milling time led to the improvement of reinforcement distribution, the increase of relative density and grain refinement. All of them should contribute to a simultaneous increase in strength and ductility. However, the elongation of the composite showed an overall tendency to decrease with increasing ball milling time, except for a turnaround at 20 h.

According to previous studies, the effects of ball milling time on the ductility of composites prepared by powder metallurgy are controversial. Liu et al. [46] found that the elongation of CNT/Al composite increased when the ball milling time increased from 2 to 6 h, which was mainly attributed to the improved dispersion of

the reinforcements. The increase in ball milling time from 6 h to 12 h resulted in a decrease in elongation, which was associated with the damage of the CNTs and the introduction of impurities (Fe, $Al_2O_3$). Lou et al.[47] [42] investigated the effect of the ball milling process on the mechanical properties of GNPs/Al. They found similar results to Liu et al. [46], i.e., the elongation of the composite increased and then reduced as the ball milling time increased from 2 h to 8 h. The decrease in elongation was mainly related to the damage of the GNPs. While Zheng et al. [48] reported that when the ball milling time increased from 0 h to 20 h, the elongation of Al2024 alloy decreased continuously. This was mainly due to the formation of oxides and porosity. Moreover, Yu et al. [49] found that as ball milling time increased, the elongation of the matrix decreased first from 18.3% (milled for 1h) to 14% (milled for 3h), and then increased rapidly to 25.6% (milled for 4h). A similar trend in elongation was observed in the ball-milled composites. The author thought the greatly enhanced elongation might be due to the lamellar structure introduced by flake-shape powders.

As shown in Fig. 9, no structural damage occurred to TiC nanoparticles after ball milling for 20 h. In addition, the TiC/AZ61 composite's porosity decreased with the ball milling time. It can therefore be speculated that the increase in ball milling time leading to a reduction in elongation in this study may be associated with the introduction of impurities and oxides. The unusual variation in elongation at 20 h should be mainly related to its microstructure, which will be discussed in detail in Discussion 4.5.

### 4.3. Strengthening mechanisms

As is known to all, the improved strength of PRMMC can be attained by four possible strengthening mechanisms, including grain boundary strengthening through Hall-Petch relationship ($\Delta\sigma_{Hall-Petch}$), dislocation strengthening induced by different thermal expansion coefficients ($\Delta\sigma_{CTE}$), load transfer strengthening ($\Delta\sigma_{load}$) and Orowan strengthening ($\Delta\sigma_{Orowan}$). Thus, the increment of YS can be evaluated by considering the multiple strengthening mechanisms:

$$\Delta\sigma_c = \Delta\sigma_{Hall-Petch} + \Delta\sigma_{CTE} + \Delta\sigma_{load} + \Delta\sigma_{Orowan} \quad (1)$$

The increase in yield strength resulting from grain refinement can usually be calculated by the Hall-Petch formula, which is expressed as follows [50]:

$$\Delta\sigma_{Hall-Petch} = K(d_c^{-\frac{1}{2}} - d_m^{-\frac{1}{2}}) \quad (2)$$

where $K$ is the Hall-petch slope, $K$= 0.13 MPa $m^{1/2}$ for the Mg， $dc$ and $dm$ are the average grain size of the composite and matrix, respectively. Grain refinement is caused by TiC nanoparticle addition and ball milling. The average grain size of AZ61, 20 h and 30 h ball milled composites is 10.23 μm, 3.44 μm and 2.06 μm,

respectively. The $\Delta\sigma_{Hall-Petch}$ for 20 h and 30 h ball milled composites is calculated to be 29.6 and 50.0 MPa, respectively.

Thermal mismatch strengthening is mainly because of the different thermal expansion coefficients between the metal matrix and the reinforcement, leading to the increase of dislocation density near its interface. Its contribution to the yield strength can be expressed as [51]:

$$\Delta\sigma_{CTE} = \sqrt{3}\beta Gb\sqrt{12\frac{\Delta\alpha\Delta T V_p}{(1-V_p)bd_p}} \quad (3)$$

where $\beta$ is a constant (1.25), $G$ is the shear modulus of matrix (16.6GPa), $b$ is the Burgers vector (0.32 nm). $\Delta\alpha$ is the difference in the coefficient of thermal expansion between the TiC particles and AZ61 matrix ($2.38\times10^{-5}$ $K^{-1}$), $\Delta T$ is the difference between the hot extrusion temperature and the mechanical properties test temperature of the composites (325 K), $V_p$ is the volume fraction of the reinforcement (0.36 vol.%), $d_p$ is the diameter of the reinforcing particles (50 nm). Thus, according to Eq. 3, the contribution of thermal mismatch strengthening to yield strength is 52.7 MPa.

The load-bearing effect is the transfer of load from the matrix to the reinforcement by interfacial shear stress during tension. It can be evaluated using the modified shear lag model, which is expressed as the following equation [52]:

$$\Delta\sigma_{load} = 0.5SV_p\sigma_m \quad (4)$$

where $S$ is the aspect ratio of reinforcement, $\sigma_m$ is the yield strength of the matrix. For the TiC nanoparticle, S is about 1. $\Delta\sigma_{load}$ is calculated as 0.4 MPa. Therefore, the contribution of $\Delta\sigma_{load}$ to the increase in YS can be ignored.

In Orowan mechanism, the magnitude of nanoparticles contribution is significantly higher than that of micron particles. Therefore, for nanoparticles, Orowan mechanism usually play a very important role in improving the yield strength of composites. The following Orowan-Ashby equation can express this contribution to YS [53]:

$$\Delta\sigma_{Orowan} = \beta\frac{0.4Gb}{\pi\sqrt{1-\nu}}\frac{\ln(\bar{d}/b)}{\lambda} \quad (5)$$

where $\nu$ is Poisson's ratio for Mg (0.35), $G$, $b$ and $d_p$ are the same defined above. $\lambda$ is interparticle spacing, which can be calculated by the following equation [9]:

$$\lambda = \bar{d}(\sqrt{\pi/4V_p} - 1) \quad (6)$$

where $\bar{d} = \sqrt{2/3}d_p$. Therefore, the increased YS attributed to $\Delta\sigma_{Orowan}$ is calculated to be 8.6 MPa.

Based on the previous microstructure analysis, the increase in the ball milling time mainly improved reinforcement distribution and enhanced grain refinement. This helps to enhance the contribution of grain boundary strengthening and Orowan strengthening. According to Eq. 3, if the volume fraction of the reinforcement was fixed, the value of $\Delta\sigma_{CTE}$ was fixed. Therefore, the increase in ball milling time had no effect on the thermal mismatch strengthening theoretically. For the Orowan strengthening, Eqs. 5 and 6 were used, assuming the reinforcement was uniformly distributed. Based on the analysis in Discussion 4.2 and Fig. 5 (t), it can be considered that the 30 h composite material achieved the most uniform dispersion, so its actual $\Delta\sigma_{Orowan}$ was closest to the theoretical value. By calculating the sum of the contributions of grain refinement strengthening, thermal mismatch strengthening and Orowan strengthening, it can be seen that the increased yield strength of 30 h nanocomposite based on theoretical calculation was 111.3 MPa. However, the experimental result (342.2 MPa) of the yield strength of the nanocomposite was 23.6 MPa higher than the calculated values (318.6 MPa). This can be attributed to the presence of high amount of the fine β-$Mg_{17}Al_{12}$ precipitates and some Al-Mn nanophases, both capable of enhancing the strength of composites. However, the strengthening effects from these phases were not considered in theoretical calculations.

### 4.4. Extra strengthening of HBG composite at UTS

According to the previous microstructure analysis, the heterostructure TiC/AZ61 composite consisted of particle-rich FG zones and particle-rare CG bands. Based on the nanoindentation results in Fig. 11 (d) and Table 3, the particle-rich FG zone had higher hardness and modulus than the particle-rare CG band in the HBG composite. Thus, particle-rich FG zones and particle-rare CG bands can be regarded as "hard" unit and "soft" regions, respectively. The heterogeneous composite can be considered as consisting of "hard" unit and "soft" regions. The rule-of mixture can be applied to calculate the strength of such a heterogeneous composite [11]:

$$\sigma_{Bimodal} = \sigma_{CG}V_{CG} + \sigma_{FG}V_{FG} \quad (7)$$

$$= \sigma_{CG}V_{CG} + \sigma_{FG}(1 - V_{CG}) = (\sigma_{CG} - \sigma_{FG})V_{CG} + \sigma_{FG} \quad (8)$$

where $V_{CG}$ and $V_{FG}$ are the volume fractions of the CG and FG zones, respectively; $\sigma_{CG}$ and $\sigma_{FG}$ are the strengths of the CG and FG zones, respectively.

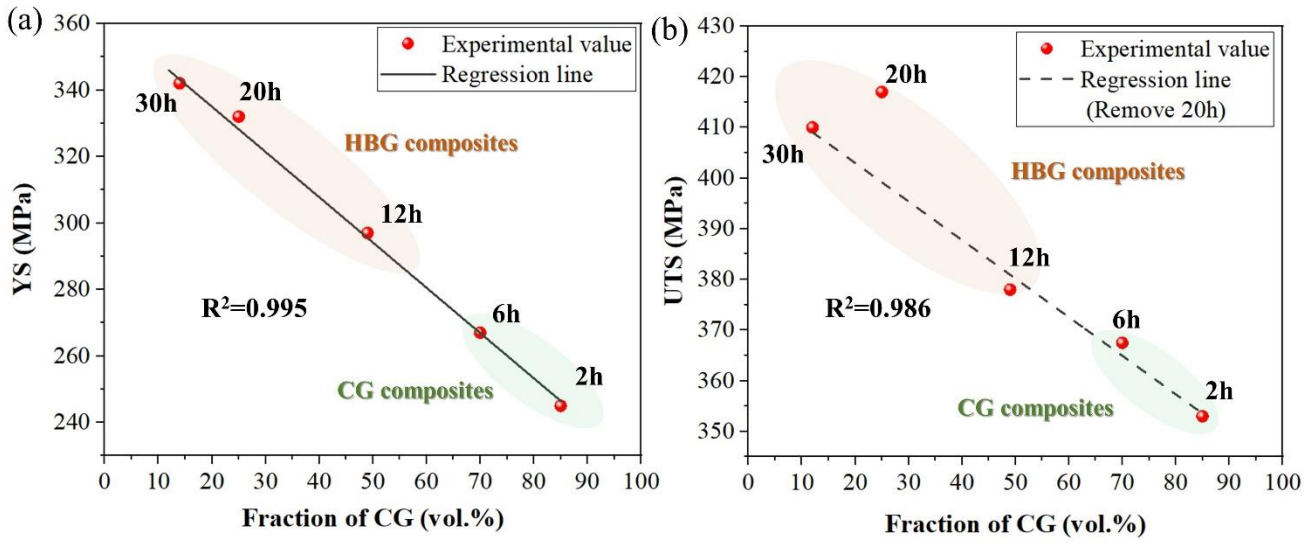


**Fig. 13.** The experimental strength value and regression lines of TiC/AZ61 composites: (a) YS and (b) UTS.

Based on the rule-of-mixtures (Eq. (7) and (8)), the CG fraction of the composite should have a negative linear relationship with its strength (YS and UTS). In other words, the strength values of composites at different CG fractions should be able to be fitted to a straight line. Specifically, the strength of the composite increased monotonically as the CG fraction decreased. The red dots in Fig. 13 are the experimental values of different composites, and the solid black lines are their regression lines fitted by the red dots. As can be seen from Fig. 13 (a), the predicted YS was very close to the experimental value, and the $R^2$ value was 0.984. The closer the value of $R^2$ is to 1, the better the fit of the regression line to the observed value. The dashed line in Fig. 13 (b) represents the regression line obtained after removing the 20 h experimental value. It is worth noting that other experimental values are very close to the regression line, while the experimental value of 20 h is much higher than the regression line. This indicates that there was an extra strengthening in the HBG-20 h composite.

It was reported that, inverse nacre structured composite [5], heterogeneous bimodal grain structure [11] and heterogeneous lamellar grain [54] composites could produce an intrinsic synergetic strengthening effect. Their actual strength was even higher than the sum of the strength of individual components, as calculated by the rule-of-mixtures. The mechanism for the extra strengthening obtained by heterogeneous composites was mainly associated with hetero-deformation induced (HDI) strengthening. It is derived from the strain gradient in the near-interface region generated by different components with mechanical incompatibility to coordinate deformation under uniaxially applied stress. For the HBG-20 h composite, a large difference in mechanical properties existed between the CG band and the FG zone, as evidenced by the nanoindentation results (Fig. 11 (d)). As a result, the FG zones and CG bands could induce severe mechanical incompatibility during deformation,

resulting in synergistic constraints between them. This constraint contributed to the accumulation of strain gradient near the CG/FG interfaces.

At the early stage of plastic deformation, the deformation incompatibility between the CG and FG regions was not significant. The YS of heterogeneous composites could conform well to the regression line (Fig. 13(a)). With the plastic deformation proceeding, the deformation incompatibility increased continuously. A large number of geometrically necessary dislocations (GNDs) generated near those heterogeneous interfaces to accommodate deformation gradients and satisfy the compatible deformation [55]. These GNDs generally arose on the side of the coarse grains near the CG-FG interface, resulting in the coarse grains being strengthened by the back stress strengthening mechanism [11, 54], thus providing additional strengthening to the heterogeneous composites. The back stress strengthening of the HBG-20 h composite could be verified by the formation of GNDs in Fig. 14 (a). Consequently, the UTS of the HBG-20 h composite was higher than the predicted value (Fig. 13 (b)).

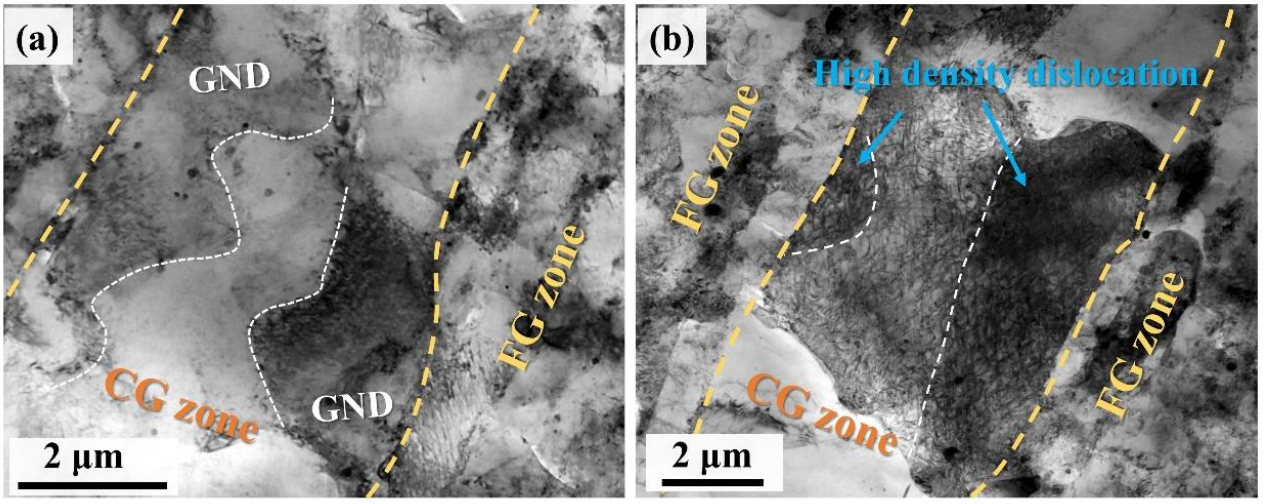


**Fig. 14.** TEM images for the HBG-20 h composite after a tensile strain of 7%. (a) Dislocation pile-ups in the CG zone adjacent to the FG zone, its outline is marked with a white dashed line. (b) A high density of dislocations inside the CG zone.

The back stress strengthening depended on the thickness of the strain gradient layer and the number of heterogeneous interfaces. It is reasonable to expect that the wider the strain gradient region around the interface and the more heterogeneous interfaces generating strain gradients, the higher synergetic strengthening could be induced. Fig. 15 shows that schematic diagram of strain gradient and GND distribution in the CG bands of different HBG composites. The reasons HBG-12 h and HBG-30 h composites did not obtain additional back-stress strengthening were considered from the following two aspects. (i) The thickness of the strain gradient

layer depended on the variability degree of two components on both sides of the interface. As the FG surrounded the CG band in HBG-20 h (Fig. 15(b)) and HBG-30 h composite (Fig. 15(c)), the deformation of the CG bands was constrained, leading to the generation of strain gradient layers in the heterogeneous composites during deformation. However, the CG bands were adjacent or connected in HBG-12 h composites (Fig. 15(a)), they were difficult to be restrained by the FG zone. Therefore, the strain gradient layer did not generate or was very thin. This means that thick strain-gradient layers require that the CG content was not too high and the CG bands were uniformly distributed and unconnected. (ii) Number of CG/FG interfaces. The more CG bands were bounded by the FG, the stronger the back-stress strengthening effect. It implies that the content of CG bands was not too low. In summary, almost no back-stress strengthening was obtained in the HBG-12 h and HBG-30 h composites because of the high content of CG bands (48.4%) and the contact and connection between CG bands in the HBG-12 h composite, and the low content of CG bands (11.7%) in the HBG- 30 h composite.

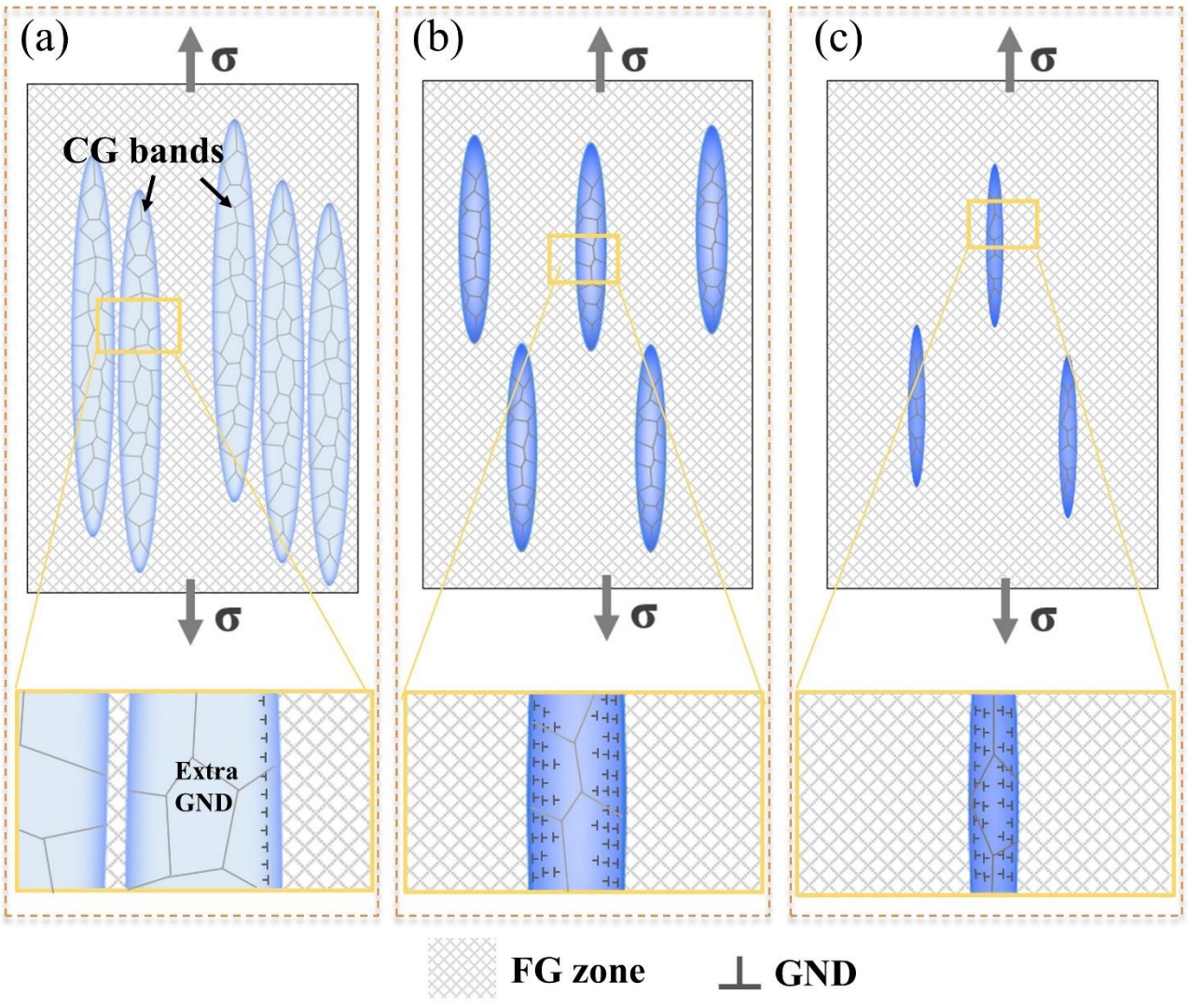

**Fig. 15.** Schematic diagram of strain gradient and GND distribution in the CG bands of different HBG composite: (a) HBG-12 h, (b) HBG-20 h, (c) HBG-30 h. The color blue and its contrast were used to represent strain gradient qualitatively.

### 4.5. Effect of HBG structure on the ductility of composites

As seen in Fig. 11 (b) and (e), the HBG-20 h composite showed a combination of high strength and good ductility. The mechanism responsible for the improvement of ductility for HBG structure composites was discussed based on the following aspects:

(i) Normally, the failure of materials is associated with necking or localized deformation, while a high work hardening ability can effectively distribute plastic deformation to achieve more uniform elongation. The strength difference ($\Delta\sigma_{hard}$ = UTS - YS) was used to evaluate the hardening ability of the bimodal composites [56]. The $\Delta\sigma_{hard}$ values of the HBG-12 h, HBG-20 h and HBG-30 h composites were calculated as 81 MPa, 94 MPa and 68 MPa, respectively. Thus, the higher work hardening of HBG-20 h composite led to a higher ductility than the HBG-12 h and HBG-30 h composites. The higher strain hardening in HBG-20 h composite should be mainly due to the differences in their HBG structural features.

As previously reported [17,54,57], back-stress strengthening generated in heterostructure composites/magnesium alloys due to mechanical incompatibility during deformation. Zan et al. [54] prepared $Al_2O_3$ particulate reinforced Al composites with three different grain characteristics: uniform ultrafine grain, random bimodal grain, and heterogeneous lamellar grain structures. The results show that the composite with the lamellar structure had better strength and ductility than the other two composites, because this structure allowed the material to achieve the strongest back-stress strengthening. Fu et al. [17] prepared bimodal grain structure CNT/Al-Mg composites with CG fractions of 25% and 50%, named CG25 and CG50, respectively. The strain hardening of CG25 was greater than that of CG50 because the former had a lower fraction of CG and thus was more susceptible to interface-affected zone. Han et al. [57] fabricated Mg alloy with a heterogeneous gradient structure. Its unique structure could effectively develop hetero-deformation induced strengthening and dislocation hardening, thus introducing high strain hardening and good ductility.

Back-stress strengthening improves strain-hardening capacity, which could be explained by the following two aspects. (1) the GND provided additional dislocations, facilitating the accumulation of more dislocations. (2) the GNDs pile-up near the interface zone produced long-range back stress to prohibit further dislocation emission from the dislocation source, improving back stress hardening [58]. Fig. 15 (b) shows a high density of

dislocations piled up inside the coarse grain. Especially, near the CG/FG interface region (marked by blue arrows), confirming that back-stress strengthening contributed to the accumulation of higher-density dislocations. Therefore, the higher strain hardening for HBG-20 h composites should be mainly due to the contribution of its higher back-stress strengthening.

(ii) The transfer and redistribution of local strain also play an important role in improving the ductility of HBG composites. It is well known that cracks preferentially initiate in those areas with severe stress concentration. According to the void growth model of Rice and Tracey [59], the higher the strain, the faster the void growth, leading to a more rapid fracture of the material. Therefore, it is important to alleviate stress concentration during deformation. Some researchers used digital image correlation technology to study the strain evolution of HBG aluminum matrix composites during tensile deformation [11, 56]. It is found that because of the introduction of coarse grains, the strain localization was separated and redistributed near the heterogeneous interface, thus releasing the stress concentration. Thus, the high elongation of HBG-20 h composite may be related to its internal strain evolution and strain transfer, which may alleviate the stress concentration.

## 5. Conclusions

Heterogeneous TiC/AZ61 nanocomposites with high strength and good ductility, consisting of TiC-free coarse grain (CG) bands and TiC-rich fine grain (FG) zones, were fabricated in this study. The fraction of CG bands could be optimized by adjusting the mechanical ball milling time. Based on the microstructure analysis, mechanical properties, strengthening mechanisms, the extra-strengthening at UTS and increasing ductility mechanisms. The main conclusions are summarized as below:

(1) Adjusting the ball milling time was a controllable preparation method to obtain and further optimize the HBG structure. The powder morphology had an essential influence on the reinforcement distribution, which further affected the microstructure of the final composite. Therefore, the fraction of CG bands in the HBG composite could be controlled by regulating the ball milling time to change the proportion of powders with different morphologies.

(2) When the ball milling time increased from 2 h to 6 h, the microstructure of the composites was composed mainly of coarse grains. With the ball milling proceeding from 12 h to 30 h, the microstructure of the composites consisted of a high number of FG zones and some CG bands (i.e., HBG structure). Nano-TiC particles were rich in the FG region but rare in the CG band. In addition, with the increase of milling time from

12 h to 30 h, the proportion of spherical powder decreased, so the fraction of CG bands in the final composite decreased.

(3) With the increase of ball milling time, the YS increased continuously, while UTS first increased from 2 h to 20 h and then decreased at 30 h. The elongation did not show a monotonous downward trend but presented an inflection point at 20 h. As a result, excellent comprehensive mechanical properties (ultimate tensile strength: 417 MPa, yield strength: 323 MPa, and elongation: 10.2%) were achieved in the composites with ball milling for 20 h. The increase in yield strength was mainly attributed to the grain refinement, thermal mismatch strengthening and Orowan strengthening mechanism.

(4) The HBG-20 h composite obtained significant additional strengthening at UTS. It is because mechanical incompatibility between the TiC-rare CG band and TiC-rich FG zone led to the formation of a large amount of GND in the near-interface region during the deformation process, thus providing back-stress work hardening to the composite. Moreover, optimal back-stress work hardening was achieved in HBG-20 h composite due to its suitable CG band fraction (~ 25 vol.%). This also contributed to the high strain hardening, thus improving the composite's ductility.

## Acknowledgement

This work was supported by China Scholarship Council (No. 202107000038).

## Data availability

The raw/processed data required to reproduce these findings cannot be shared at this time as the data also forms part of an ongoing study.

## References


[1] Casati R, Vedani M, Metal matrix composites reinforced by nanoparticles – a review. Metals 2014;4(1):65-83.

[2] Arunachalam R, Krishnan PK, Muraliraja R. A review on the production of metal matrix composites through stir casting – Furnace design, properties, challenges, and research opportunities. J Manuf Processes 2019;42:213-245.

[3] Nie KB, Wang XJ, Deng KK, Hu XS, Wu K. Magnesium matrix composite reinforced by nanoparticles – A review. J Magnesium Alloys 2021;9(1):57-77.

[4] Sardar S, Karmakar SK, Das D. Ultrasonic Assisted Fabrication of Magnesium Matrix Composites: A Review. Mater Today Proc 2017;4(2):3280-3289.

[5] Luo X, Zhao K, He X, Bai YL, Andrade VD, Zaiser M, et al. Evading strength and ductility trade-off in an inverse nacre structured magnesium matrix nanocomposite. Acta Mater 2022;228: 117730-117744.

[6] Salama EI, Morad SS, Esawi AMK. Fabrication and mechanical properties of aluminum-carbon nanotube functionally-graded cylinders. Materialia 2019;7:100351-100358.

[7] Li Z, Guo Q, Li ZQ, Fan GL, Xiong DB, Su YS, et al. Enhanced mechanical properties of graphene (reduced graphene oxide)/aluminum composites with a bioinspired nanolaminated structure. Nano Lett. 2015;15(12):8077-8083.

[8] Shu R, Jiang XS, Sun HL, Shao ZY, Song TF, Luo ZP. Recent researches of the bio-inspired nano-carbon reinforced metal matrix composites. Composites Part A 2020;131:105816-105838.

[9] Jiang L, Yang H, Yee JK, Mo X, Troy T, Lavernia EJ, et al. Toughening of aluminum matrix nanocomposites via spatial arrays of boron carbide spherical nanoparticles. Acta Mater 2016;103(15):128-140.

[10] Zha M, Zhang HM, Yu ZY, Zhang XH, Meng XT, Wang HY, et al. Bimodal microstructure – A feasible strategy for high-strength and ductile metallic materials. J Mater Sci Technol 2018;34(2):257-264.

[11] Liu ZY, Ma K, Fan GH, Zhao K, Zhang JF, Xiao BL, et al. Enhancement of the strength-ductility relationship for carbon nanotube/Al-Cu-Mg nanocomposites by material parameter optimization. Carbon 2020;157:602-613.

[12] Ma K, Liu ZY, Liu K, Chen XG, Xiao BL, Ma ZY. Structure optimization for improving the strength and ductility of heterogeneous carbon nanotube/Al-Cu-Mg composites. Carbon 2021;178(30):190-201.

[13] Wang HY, Yu ZP, Zhang L, Liu CG, Zha M, Wang C, et al. Achieving high strength and high ductility in magnesium alloy using hard-plate rolling (HPR) process. Sci Rep 2015, 5:17100-17109.

[14] Zhang H, Wang HY, Wang JG, Rong J, Zha M, Wang C, et al. The synergy effect of fine and coarse grains on enhanced ductility of bimodal-structured Mg alloys. J Alloys Compd 2019;780(5):312-317.

[15] Xiang SL, Wang XJ, Gupta M, Wu K, Hu XS, Zheng MY. Graphene nanoplatelets induced heterogeneous bimodal structural magnesium matrix composites with enhanced mechanical properties. Sci Rep 2016;6:38824-38827.

[16] Shen MJ, Wang XJ, Zhang MF, Zheng MY, Wu K. Significantly improved strength and ductility in bimodal-size grained microstructural magnesium matrix composites reinforced by bimodal sized SiCp over traditional magnesium matrix composites. Compos Sci Technol 2015;118 (30):85-93.

[17] Fu XW, Yu ZY, Tan ZQ, Fan GL, Li PF, Wang MJ, et al. Enhanced strain hardening by bimodal grain structure in carbon nanotube reinforced Al-Mg composites. Mater Sci Eng A 2021;803:140726-140738.

[18] Ren LB, Zhou MY, Lu TH, Fan LL, Guo YY, Zhang YWX, et al. Eutectic phase strengthening and strain rate sensitivity behavior of AZ80 magnesium alloy. Mater Sci Eng A 2020;770:138548-138558.

[19] Huang SJ, Subramani M, Chiang CC. Effect of hybrid reinforcement on microstructure and mechanical properties of AZ61 magnesium alloy processed by stir casting method. Compos Commun 2021;25:100772-100779.

[20] Pan FS, Feng ZX, Zhang XY, Tang AT. The types and distribution characterization of Al-Mn phases in the AZ61

magnesium alloy. Procedia Eng 2012;27:833-839.
[21]Sarvesha R, Ghori U, Chiu YL, Jones IP, Singh SS, Jain J. Mechanical property evaluation of second phase particles in a Mg-8Al-0.5Zn alloy using micropillar compression. Mater Sci Eng A 2020;775:138973-138978.
[22]J.T. Hou, W.B. Du, G. Parande, M. Gupta, S. Li. Significantly enhancing the strength + ductility combination of Mg-9Al alloy using multi-walled carbon nanotubes. J Alloys Compd 2019;790:974-982.
[23]Pérez-Prado MT, Del Valle JA, Ruano OA. Effect of sheet thickness on the microstructural evolution of an Mg AZ61 alloy during large strain hot rolling. Scr Mater 2004;50(5):667-671.
[24]Nie KB, Guo YC, Munroe P, Deng KK, Kang XK. Microstructure and tensile properties of magnesium matrix nanocomposite reinforced by high mass fraction of nano-sized particles including TiC and $MgZn_2$. J Alloys Compd 2020, 819:153348-153363.
[25]Nie KB, Zhu ZH, Deng KK, Han JG. Effect of extrusion temperature on microstructure and mechanical properties of a low-alloying and ultra-high strength Mg-Zn-Ca-Mn matrix composite containing trace TiC nanoparticles. J Magnesium Alloys 2020;8:676-691.
[26]Nie KB, Zhu ZH, Munroe P, Deng KK, Han JG. Effect of extrusion speed on mixed grain microstructure and tensile properties of a Mg-2.9Zn-1.1Ca-0.5Mn nanocomposite reinforced by a low mass fraction of $TiC_p$. Mater Sci Eng A 2020;796:140223-140237.
[27]Xu ZY, Fang CF, Wang R, Zhong CY, Wang YM. Microstructural evolution, strengthening and toughening mechanisms of AZ80 composite sheet reinforced by $TiB_2$ with fiber-like distribution. J Alloys Compd 2021;877:160278-160289.
[28]Xiao P, Gao YM, Yang CC, L YF, Huang XY, Liu QK, et al. Strengthening and toughening mechanisms of Mg matrix composites reinforced with specific spatial arrangement of in-situ $TiB_2$ nanoparticles. Composites Part B 2020;198:108174-108188.
[29]Sahoo BN, Panigrahi SK. Effect of in-situ (TiC-$TiB_2$) reinforcement on aging and mechanical behavior of AZ91 magnesium matrix composite. Mater Charact 2018;139:221-232.
[30]Guo YC, Nie KB, Kang XK, Deng KK, Han JG, Zhu ZH. Achieving high-strength magnesium matrix nanocomposite through synergistical effect of external hybrid (SiC+TiC) nanoparticles and dynamic precipitated phase. J Alloys Compd 2019;771:847-856.
[31]Niu XF, Li G, Zhang ZY, Zhou PW, Wang HX, Zhang SX, et al. Simultaneously improving the strength and ductility of extruded bimodal size $SiC_p$/AZ61 composites: Synergistic effect of micron/nano $SiC_p$ and submicron $Mg_{17}Al_{12}$ precipitates. Mater Sci Eng A 2019; 743:207-216.
[32]Zhou MY, Ren LB, Fan LL, Tun KS, Gupta M, Zhang YWX, et al. Achieving ultra-high strength and good ductility in AZ61 alloy composites containing hybrid micron SiC and carbon nanotubes reinforcements. Mater Sci Eng A 2019;768:138447-138460.
[33]Shen MJ, Wang XJ, Zhang MF, Hu XS, Zheng MY, Wu K. Fabrication of bimodal size $SiC_p$ reinforced AZ31B magnesium matrix composites. Mater Sci Eng A 2014;601:58-64.
[34]Rashad M, Pan FS, Guo W, Lin H, Asif M, Irfan M. Effect of alumina and silicon carbide hybrid reinforcements on tensile, compressive and microhardness behavior of Mg-3Al-1Zn alloy. Mater Charact 2015;106:382-389.
[35]Nie KB, Deng KK, Wang XJ, Wang T, Wu K. Influence of SiC nanoparticles addition on the microstructural evolution and mechanical properties of AZ91 alloy during isothermal multidirectional forging. Mater Charact 2017;124:14-24.
[36]Qiao XG, Ying T, Zheng MY, Wei ED, Wu K, Hu XS. Microstructure evolution and mechanical properties of nano-SiCp/AZ91 composite processed by extrusion and equal channel angular pressing (ECAP). Mater Char 2016;121:222-230.
[37]Li CP, Wang ZG, Wang HY, Zhu X, Wu M, Jiang QC. Fabrication of nano-SiC particulate reinforced Mg-8Al-

1Sn composites by powder metallurgy combined with hot extrusion. J Mater Eng Perform 2016;25:255049-255054.

[38]Rashad M, Pan FS, Zhang JY, Asif M. Use of high energy ball milling to study the role of graphene nanoplatelets and carbon nanotubes reinforced magnesium alloy. J Alloys Compd 2015;646:223-232.

[39]Shimizu Y, Miki S, Soga T, Itoh I, Todoroki H, Hosono T, et al. Multi-walled carbon nanotube-reinforced magnesium alloy composites. Scr Mater 2008;58:267-270.

[40]Yuan QH, Qiu ZQ, Zhou GH, Zeng XS, Luo L, Rao XX, et al. Interfacial design and strengthening mechanisms of AZ91 alloy reinforced with in-situ reduced graphene oxide. Mater Char 2018;138: 215-228.

[41]Yuan QH, Zeng XS, Liu Y, Luo L, Wu JB, Wang YC, et al. Microstructure and mechanical properties of AZ91 alloy reinforced by carbon nanotubes coated with MgO. Carbon 2016;96:843-855.

[42]Hou JT, Du WB, Parande G, Gupta M, Li S. Significantly enhancing the strength + ductility combination of Mg-9Al alloy using multi-walled carbon nanotubes. J Alloys Compd 2019, 790:974-982.

[43]Yuan QH, Zhou GH, Liao L, Liu Y, Luo L. Interfacial structure in AZ91 alloy composites reinforced by graphene nanosheets. Carbon 2018;127:177-186.

[44]Xiang SL, Hu XS, Wang XJ, Wang LD, W K. Precipitate characteristics and synergistic strengthening realization of graphene nanoplatelets reinforced bimodal structural magnesium matrix composites. Mater Sci Eng A 2018;724:348-356.

[45]Wang M, Zhao Y, Wang LD, Zhu XP, Wang XJ, Sheng J, et al. Achieving high strength and ductility in graphene/magnesium composite via an in-situ reaction wetting process. Carbon 2018;139:954-963.

[46]Liu ZY, Xu SJ, Xiao BL, Xue P, Wang WG, Ma ZY. Effect of ball-milling time on mechanical properties of carbon nanotubes reinforced aluminum matrix composites. Composites Part A 2012;43:2161-2168.

[47]Lou SM, Qu CD, Guo GX, Ran LW, Liu YQ, Zhang PP. Effect of Fabrication Parameters on the Performance of 0.5 wt.% Graphene Nanoplates-Reinforced Aluminum Composites. Materials. 2020;13(16):3483-3503.

[48]Zheng RX, Ma FM, Xiao WL, Ameyama K, Ma CL. Achieving enhanced strength in ultrafine lamellar structured Al2024 alloy via mechanical milling and spark plasma sintering. Mater Sci Eng A 2017;687:155-163.

[49]Yu ZH, Yang WS, Zhou Chang, Zhang NB, Chao ZL, Liu H, et al. Effect of ball milling time on graphene nanosheets reinforced Al6063 composite fabricated by pressure infiltration method. Carbon 2019;141: 25-39.

[50]Li CD, Wang XJ, Liu WQ, Shi HL, Ding C, Hu XS. Microstructure and strengthening mechanism of carbon nanotubes reinforced magnesium matrix composite. Mater Sci Eng A 2014;597:264-269.

[51]Goh CS, Wei J, Lee LC, Gupta M. Properties and deformation behaviour of Mg-$Y_2O_3$ nanocomposites. Acta Mater 2007;55:5115-5121.

[52]Nardone VC, Prewo KM. On the strength of discontinuous silicon carbide reinforced aluminum composites. Scr Metall 1986;20:43-48.

[53]Kim C, Sohn I, Nezafati M, Ferguson JB, Schultz BF, Bajestani-Gohari Z, et al. Prediction models for the yield strength of particle-reinforced unimodal pure magnesium (Mg) metal matrix nanocomposites (MMNCs). J Mater Sci 2013;48:4191-4204.

[54]Zan YN, Zhou YT, Liu ZY, Ma GN, Wang D, Wang QZ. Enhancing strength and ductility synergy through heterogeneous structure design in nanoscale $Al_2O_3$ particulate reinforced Al composites. Mater Des 2019;166: 107629-107637.

[55]Ashby MF. The deformation of plastically non-homogeneous materials. Philos Mag 1970;21: 399-424.

[56]Ma K, Liu ZY, Liu BS, Xiao BL, Ma ZY. Improving ductility of bimodal carbon nanotube/2009Al composites by optimizing coarse grain microstructure via hot extrusion. Composites Part A 2021;140:106198-106208.

[57]Han J, Sun JP, Song YM, Xu BQ, Yang ZQ, Xu SS. Achieving gradient heterogeneous structure in Mg alloy for excellent strength-ductility synergy. J Magnesium Alloys In Press.

[58] Wu XL, Zhu YT. Heterogeneous materials: a new class of materials with unprecedented mechanical properties. Mater Res Lett 2017;5 (8):527-532.
[59] Rice JR, Tracey DM. On the ductile enlargement of voids in triaxial stress fields. J Mech Phys Solids 1969;17(3): 201-217.